Journal of Clean Energy Technologies, Vol. 6, No. 3, May 2018

A DSP-Based Implementation of a Hybrid Solar and Wind Turbine Power Conversion System

Bao-Sheng Wang, Chen-Yao Liu, Kuo-Bin Liu, and Yuan-Chen Chien

***Abstract*—In this paper is designed and implemented a solar and wind turbine hybrid power generation system. That can be divided into the following parts, the wind turbine utilizes a three-phase switch-mode rectifier (SMR) while the solar power employs a DC/DC boost power converter together to improve the input power factor and minimize the input current harmonics distortion. This hybrid power generation system working with the perturb-and-observe algorithm Maximum Power Point Tracking (MPPT) strategy is capable of achieving robust optimum power output in working condition. Besides, to balance the DC bus and stabilize the output power, the battery system is adopted and incorporated in the hybrid system. The battery system uses a buck/boost dc chopper as the charge and discharge circuit. In the output stage, a single-phase full-bridge inverter employs the sinusoidal pulse width modulation (SPWM) strategy to generate a single-phase 60 Hz AC source to the load. The hybrid generation system is realized by using a digital signal processor (DSP) as a centralized controller to all the switching unit, and to verify the validity of the proposed architecture by recording the day-based power variation of the hybrid power system.**

***Index Terms*—Solar, wind turbine, maximum power point tracking, switch-mode rectifier, DSP.**

I. Introduction

With the increasing risk of climate changes to our living environment and possibility of crude oil depletion sooner than expected since the start of industrial revolution, countries around the world are demanding renewable energy as alternative to the fossil energy which is not enduring but also polluting the world's environment. In order to utilize the alternative energy sources, like solar, wind and tidal wave and others, efforts have been made to harness these power sources as renewable energy. Due to the current technology advances, it is becoming more feasible to utilize these renewable energy in a more efficient way to reduce our dependence on fossil oil as the major energy source to reverse the ever-increasing trend of deterioration of world environment.

For most of the countries, which relying on import of fossil oil, are desperate in need to harness the possible solar, wind and other natural energy sources as alternative energy. Especially for those areas with both excellent windy coastal lines and adequate sunshine and long sunshine duration, Combination of solar and wind turbine hybrid power generation system is a promising solution for these area.

Manuscript received Feburary 24, 2017; revised August 24, 2017.

Bao-Sheng Wang, Chen-Yao Liu, Kuo-Bin Liu and Yuan-Chen Chien are with the Power Supply Group, National Synchrotron Radiation Research Center, Taiwan (e-mail: wang.bs@nsrrc.org.tw).

Storage device like battery cells subsystem is used compensated the intermittency of solar and wind. For the hybrid system will not be limited by only one climate condition and has the advantage of harness both the solar and wind energy if properly controlled. Therefore, the hybrid power generation system accompanying the battery storage subsystem not only is capable of generating stable power to the power grids but also increasing the solar/wind power usage efficiency.

Due to the reasons mentioned above, in this paper, a solar and wind turbine hybrid power generation system is presented. The hybrid system, composed of solar and wind turbine generator together with a DC bus stabilizing battery storage system, is able to output a stable and enduring single phase AC power through the full-bridge inverter [1]-[5].

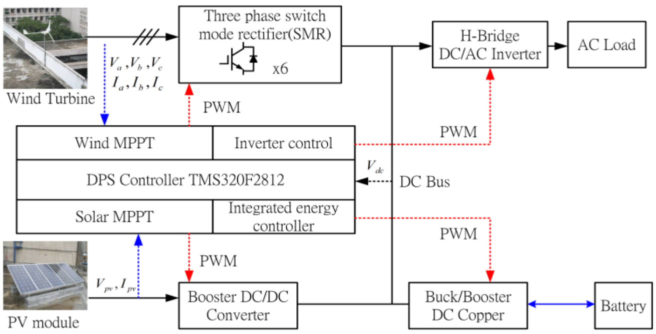

(a) System block diagram.

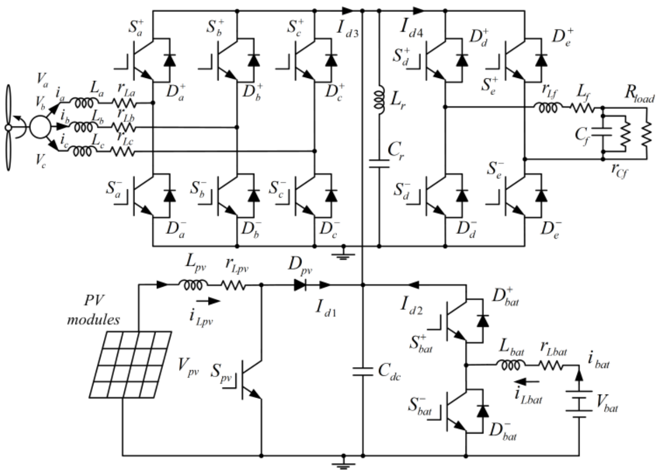

(b) Circuit architecture.

Fig. 1. Propose hybrid renewable energy generation system.

II. System Description

The system block diagram and circuit architecture of the proposed hybrid power system is depicted in Fig. 1. The whole hybrid power generation system can be divided into four major functional blocks. The first block is solar power generation which consists of five 600W Photovoltaic

doi: 10.18178/jocet.2018.6.3.469

Modules (PV) cascaded in series. The output of the PV is regulated by s DC/DC booster converter for MPPT tracking [6]-[11]. The second block is wind power generation. The wind turbine employed is a three-phases permanent magnet synchronous motor (PMSM) followed by a three-phase switch-mode rectifier (SMR) instead of the commonly used three-phase bridge rectifier to avoid the lower power factor and high current harmonic incurred by the bridge rectifier. The SMR control strategy adopted is Perturb and Observe mythology for MPPT tracking also. The third block is the battery storage circuit block. The battery storage is composed of ten 12V/17Ah lead-acid batteries cascaded together, and by working with DC voltage Buck/Boost chopper to regulate the DC bus voltage connecting the PV module and wind turbine, therefore the common DC bus can be stabilized. This battery block serves mainly to add more degree of freedom for system energy management. The last block is output inverter, which is a single-phase full-bridge inverter, combined with a second order low pass filter to deliver 110V AC source to the load. Besides, an L-C resonant circuit is implemented in the DC bus side to eliminate the second harmonic introduced by the single-phase inverter. By putting all the function blocks together, an efficient solar and wind turbine hybrid power generation system is realized.

The energy controller for the whole hybrid system is integrated into a (Digital Signal Processor) DSP. The DSP used is TMS320F2812 controller. TMS320F2812 has 16 12-Bits (Analog to Digital Converter) ADC channels, which is sufficient to acquire the system parameters in real-time for control purpose. In addition, 16 PWM channels are used to control the switching elements in the PV modules, wind turbine for MPPT tracking, and that of battery storage system for charge/discharge control and the switches of the output inverter to stabilize the power deliver to the load. The detailed circuit description in each circuit block will be presented in the following section [12], [13].

III. Circuit Analysis

A. PV Modules

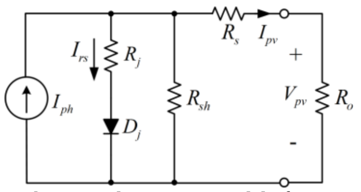

Fig. 2. The equivalent circuit model of PV module.

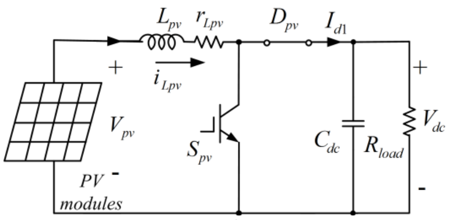

Fig. 3. The booster converter circuit for Solar power generation system.

Fig. 2 illustrates the equivalent circuit model of the PV modules. The relation of PV module's output current and output power can be expressed in (1) to (4). The DC/DC booster converter following the PV modules is shown in Fig. 3, which performs MPPT tracking by deliberately controlling the S_{pv} switch in the booster converter. Fig. 4 and Fig. 5 represent the booster converter operation mode when S_{pv} switch is off and on respectively. When S_{pv} is off, the solar energy id disconnected to the DC bus, while S_{pv} is on, solar power is delivering to the DC bus.

$$I_{pv}=n_p I_{ph}-n_p I_{rs}\left[exp\left[\frac{q}{kTA}\frac{V_{pv}}{n_s}\right]-1\right] \tag{1}$$

$$I_{rs}=I_{rr}\left[\frac{T}{T_r}\right]^3 exp\left[\frac{qEg}{kA}\left[\frac{1}{T_r}-\frac{1}{T}\right]\right] \tag{2}$$

$$I_{ph}=[I_{scr}+\alpha(T-T_r)]\frac{S}{100} \tag{3}$$

$$P_{pv}=V_{ph}n_p I_{ph}-V_{ph}n_p I_{rs}\left[exp\left[\frac{q}{kTA}\frac{V_{pv}}{n_s}\right]-1\right] \tag{4}$$

V_{pv}: PV output voltage I_{pv}: PV output current
n_s: number of series cells n_p: number of parallel cells
A: ideality factor (1~2) I_{rs}: reverse saturation current
T: junction temperature °K S: Irradiance ($\mathrm{kW/m^2}$)
k: Boltzmann's gas constant ($1.38*10^{-23}$ J/°K)
q: electronic charge ($1.6*10^{-19}$C)
α: short current coefficient

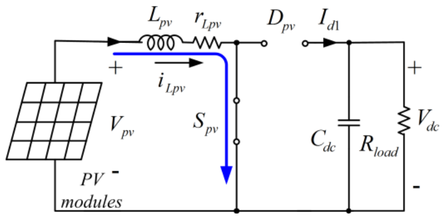

Fig. 4. S_{pv}: on operation mode.

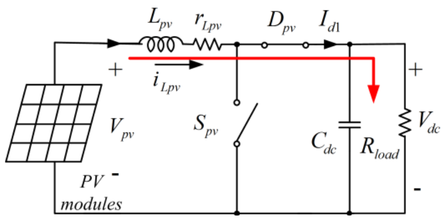

Fig. 5. S_{pv}: off operation mode.

According to KVL and KCL, the system equation of the operation mode when S_{pv} is on can be derived as

$$V_{pv}=L_{pv}\frac{di_{Lpv}}{dt}+r_{Lpv}i_{Lpv} \tag{5}$$

$$C_{pv}\frac{dV_{pv}}{dt}+\frac{V_{dc}}{R_{load}}=0 \tag{6}$$

When S_{pv}: off, the system equations expressed by (7) and (8):

$$V_{pv}=L_{pv}\frac{di_{Lpv}}{dt}+r_{Lpv}i_{Lpv}+V_{dc} \tag{7}$$

$$i_{Lpv}=C_{pv}\frac{dV_{pv}}{dt}+\frac{V_{dc}}{R_{load}} \tag{8}$$

By re-arranging (5) ~ (8), the state equation of the whole PV modules can be derived as:

$$\begin{bmatrix}\frac{di_{Lpv}}{dt}\\ \frac{dV_{dc}}{dt}\end{bmatrix}=\begin{bmatrix}-\frac{r_{Lpv}}{L_{pv}} & \frac{d_{pv}-1}{L_{pv}}\\ \frac{1-d_{pv}}{C_{dc}} & -\frac{1}{R_{load}C_{dc}}\end{bmatrix}\begin{bmatrix}i_{Lpv}\\ V_{dc}\end{bmatrix}+\begin{bmatrix}\frac{1}{L_{pv}}\\ 0\end{bmatrix} \tag{9}$$

The detailed Perturb and Observe for solar power MPPT tracking control flow is plotted in Fig. 6 [14].

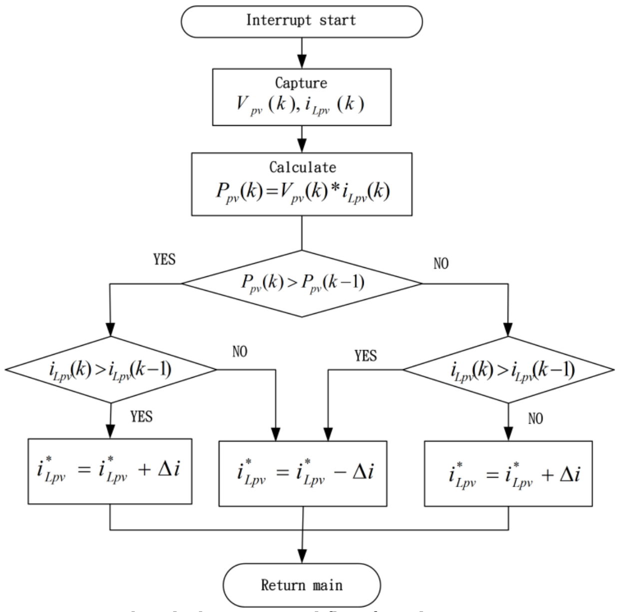

Fig. 6. Perturb and Observe control flow for solar r power generation system.

B. Wind Turbine

The wind power conversion circuit diagram is depicted in Fig. 7. The energy generated by the wind turbine is converted by a three-phase switch-mode rectifier (SMR). In comparison with the traditional AC to DC full bridge rectifier converter with the merits of simplicity and control-free, however, due to the natural characteristic of diode rectification, the wind turbine will exhibit non-continuous current and thus induce huge low harmonic current distortion. This will lower the power factor and sacrifice the power generation efficiency. To conquer these disadvantages of the traditional bridge rectifier conversion, the SMR architecture is adopted. The SMR consists of three step-up inductors, six IGBT switches with built-in free-wheel diode. The control algorithm will be explained as follows [15]-[19].

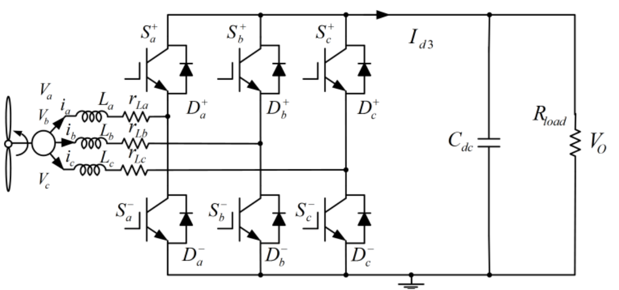

Fig. 7. Wind turbine power converter circuit.

1) SMR switching algorithm

Assuming that the input three phase voltages V_a, V_b and V_c from wind turbine to SMR are balanced. The three phase input currents will keep close track with the three phase input voltages of wind turbine. For easy explanation of the SMR working principle, the variable cycle period is divided into 6 working zones with 60 degree each. The three phase output voltages divided into 6 working zones is showed in Fig. 8.

Here, behavior of zone I is used as a working example to simplify the explanation of the SMR switching algorithm. In zone I, input voltage V_a and V_c are positive, V_b is negative. As assumed, the three phase output voltages are in phase with the output current, then the output current i_a and i_c are positive, while i_c is negative, which is the same situation with the voltages. In this zone, the current will not flow through D_a^-, D_b^+ and D_c^- and switches S_a^+, S_b^- and S_c^+. By controlling S_a^-, S_b^+ and S_c^-, where S_b^+ is always off and S_b^- is always on, hence the converter circuit is equivalent to two booster converter cascaded in parallel as shown in Fig. 9. By the analysis in zone I, the SMR circuit in Fig. 7 can be simplified and reduced to circuit in Fig. 9. The Fig. 9 can further generalized and represented by Fig. 10.

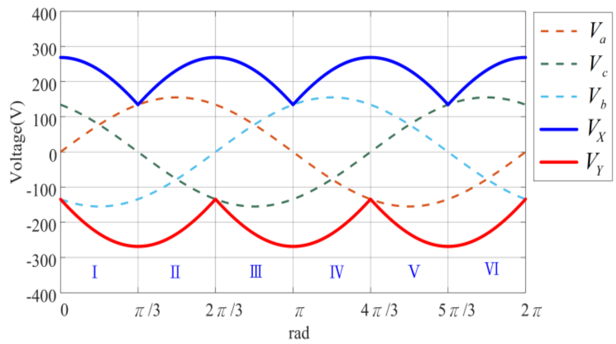

Fig. 8. Wind turbine output voltage within one cycle period divided by 6 operational zones.

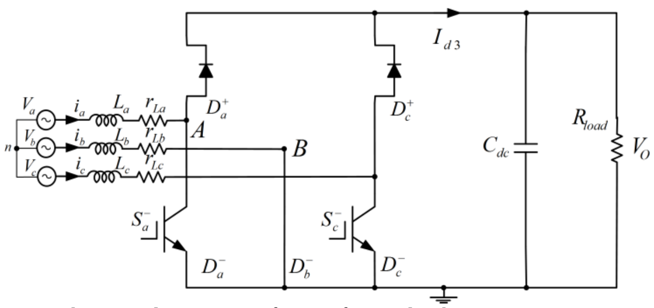

Fig. 9. The equivalents circuit of zone I for wind turbine generation system.

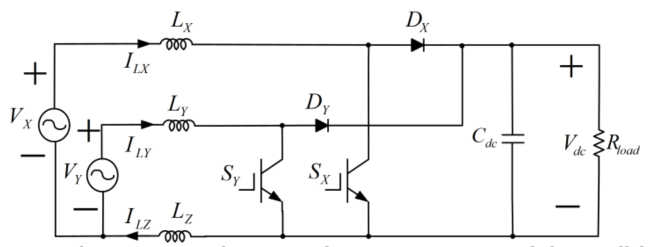

Fig. 10. The circuit equivalents to two booster converter cascaded in parallel for all zones.

With the circuit topology in Fig. 10, the voltage and current mapping for all operation zones are listed in Table I.

2) Wind turbine power factor correction algorithm:

Fig. 11 depicts the power correction algorithm of the wind turbine. When the input impedance of the equivalent circuit model of two booster converter cascaded in parallel as shown in Fig. 10 is pure resistive, the power factor will be 1. However, the input impedance is not resistive; therefore some correction method has to be adopted to modify the power factor to be close to 1 as possible. Assume that the input impedance is resistive and expressed by R_{eq}, then the relation between the voltage and current is:

$$|V_a| = R_{eq}\langle |I_a| \rangle$$

$$|V_b| = R_{eq}\langle |I_b| \rangle$$
$$|V_c| = R_{eq}\langle |I_c| \rangle$$

The V_X and V_Y in Fig. 10 is synthesized by V_{ab}, V_{bc} or V_{ca} according to the mapping list in Table I. The synthesized V_X and V_Y are used as command waveform to be followed by the desired I_{LX} and I_{LY} current command to make the power factor close to 1。The current command I_{LX_COM} and I_{LY_COM} are compared to the real I_{LX} and I_{LY} current waveform, the current waveform error (e_{r_X} and e_{r_Y}) is input to a P-I controller. The compensated command is compared to a PWM circuit to decide the on-off duty cycle of the corresponding switches in different operational zone. Table II lists the switches to be controlled on or off in the 6 operation zones.

To achieve near 1 power factor, the V_X, V_Y, I_{LX} and I_{LY} have to be chosen according to Table I, while which switches of the SMR circuit to be controlled in each zone are decided by Table II. The selected parameters from Table I are calculated according to (10) ~ (15) to derive the switching command d_X and d_Y to the switches of the SMR circuit.

TABLE I: VOLTAGE AND CURRENT MAPPING LIST FOR ALL OPERATIONAL ZONES SHOWN IN FIG. 10

	V_X	V_Y	I_{LX}	I_{LY}	I_{LZ}	S_X	S_Y	1
I	V_{ab}	V_{cb}	I_{ab}	I_{cb}	$I_{ab}+I_{cb}$	S_A^-	S_C^-	S_B^-
II	V_{ab}	V_{ac}	$-I_{ab}$	$-I_{ac}$	$-(I_{ab}+I_{ac})$	S_B^+	S_C^+	S_A^+
III	V_{bc}	V_{ac}	I_{bc}	I_{ac}	$I_{bc}+I_{ac}$	S_B^-	S_A^-	S_C^-
IV	V_{bc}	V_{ba}	$-I_{bc}$	$-I_{ba}$	$-(I_{bc}+I_{ba})$	S_C^+	S_A^+	S_B^+
V	V_{ca}	V_{ba}	I_{ca}	I_{ba}	$I_{ca}+I_{ba}$	S_C^-	S_B^-	S_A^-
VI	V_{ca}	V_{cb}	$-I_{ca}$	$-I_{ca}$	$-(I_{ca}+I_{ca})$	S_A^+	S_B^+	S_C^+

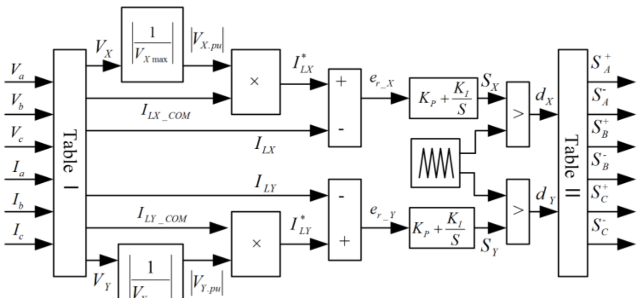

Fig. 11. Control scheme of the three-phase SMR converter.

$$I_{LX}^* = |V_{X.pu}| * I_{LX\_COM} \tag{10}$$

$$I_{LY}^* = |V_{Y.pu}| * I_{LY\_COM} \tag{11}$$

$$S_X = (I_{LX}^* - I_{LX}) * \left(K_P + \frac{K_I}{S}\right) \tag{12}$$

$$S_Y = (I_{LY}^* - I_{LY}) * \left(K_P + \frac{K_I}{S}\right) \tag{13}$$

$$S_X = \left(|V_{X.pu}| * I_{LX\_COM} - I_{LX}\right) * \left(K_P + \frac{K_I}{S}\right) \tag{14}$$

$$S_Y = \left(|V_{Y.pu}| * I_{LY\_COM} - I_{LY}\right) * \left(K_P + \frac{K_I}{S}\right) \tag{15}$$

where $|V_{X.pu}|$: absolute value of normalized V_X

$|V_{Y.pu}|$: Absolute value of normalized V_Y

I_{LX_COM}, I_{LY_COM}: Desired I_{LX}, I_{LY} command

TABLE II: SWITCHING LIST FOR ALL OPERATIONAL ZONE

Zone	A		B		C	
	S_A^+	S_A^-	S_B^+	S_B^-	S_C^+	S_C^-
I	0	d_X	0	1	0	d_Y
II	1	0	d_X	0	d_Y	0
III	0	d_Y	0	d_X	0	1
IV	d_Y	0	1	0	d_X	0
V	0	1	0	d_Y	0	d_X
VI	d_X	0	d_Y	0	1	0

As listed in Table II, there is only one switch active in each switch arm in each operational zone. This will minimize the total switching loss of the SMR circuit and thus benefit the power factor correction more efficiently. Besides, there is also no switch dead time issue in the correction algorithm, the total harmonic distortion (THD) is also reduced.

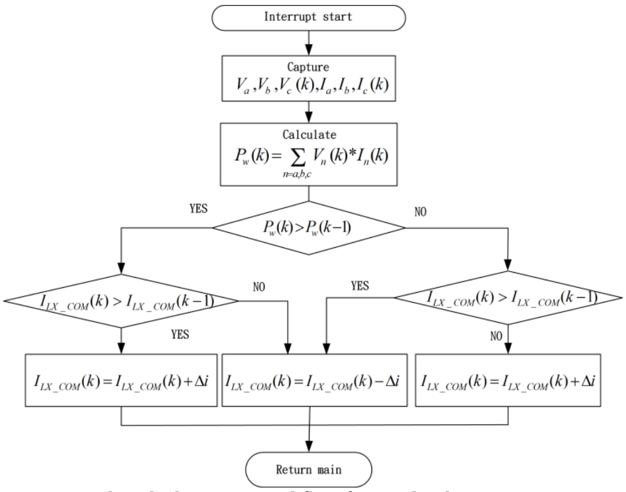

Fig. 12. Perturb and Observe control flow for wind turbine power generation system.

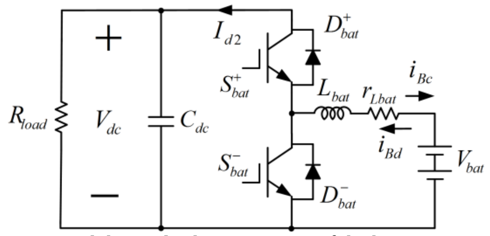
Fig. 13. Buck/boost dc chopper circuit of the battery system.

C. Battery Storage

The battery system uses a buck/boost dc chopper circuit as the charge and discharge circuit to balance the DC bus. The buck/boost dc chopper circuit of the battery system is depicted in Fig. 13. The circuit consists of a single arm IGBT switches of (S_{bat}^+, S_{bat}^-) and ripple current L-C filter. When the output powers form either the PV modules or the wind turbine is larger than the load needs. The buck/boost dc chopper will work in the buck conversion mode to store the excess energy to the battery system, while the output power generated is less than the load needs, the buck/boost dc chopper will work in the boost conversion mode to discharge the energy from the battery system onto the DC bus in order to maintain the desired DC bus voltage and hence keep the DC bus in stable condition. The equivalent circuit of the buck/boost dc chopper working in the boost and buck conversion mode is illustrated in Fig. 14. With the equivalent circuit, the corresponding equations can be derived as (16) ~ (19).

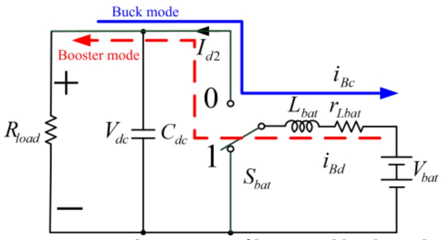

Fig. 14. Equivalent circuit of boost and buck mode.

By KVL, the discharge equation can be expressed as in (16) and (17), while in the charging equation can be derived and expressed as in (18) and (19):

$$V_{bat} = (1 - d_{boost})V_{dc} + L_{bat}\frac{di_{Bd}}{dt} + r_{Lbat}\, i_{Bd} \qquad (16)$$

$$d^{*}_{boost} = \frac{1}{V_{dc}}\left[\frac{L_{bat}}{T_s}(i^{*}_{Bd} - i_{Bd}) + V_{dc} - V_{bat}\right] \qquad (17)$$

$$d_{buck}\, V_{dc} = V_{bat} + L_{bat}\frac{di_{Bc}}{dt} + r_{Lbat}\, i_{Bc} \qquad (18)$$

$$d^{*}_{buck} = \frac{1}{V_{dc}}\left[\frac{L_{bat}}{T_s}(i^{*}_{Bc} - i_{Bc}) + V_{bat}\right] \qquad (19)$$

Fig. 15 shows the control flow chart of the buck/boost dc chopper circuit of the battery system. The algorithm reading the current DC bus and voltage V_{bat} in the start and compare it with the reference working voltage V_{ref}. As described above about the working principle of the buck/boost dc chopper circuit of the battery system. The algorithm will keep the DC bus voltage in close track with the reference voltage to stable the DC bus in order to achieve stable output power to the load [20].

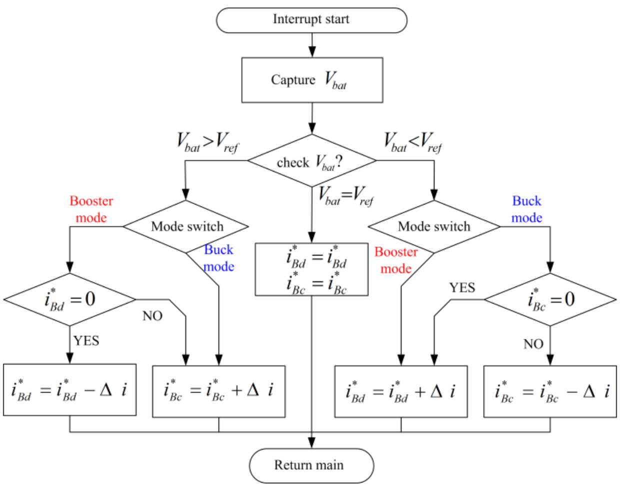

Fig. 15. Battery system's buck/boost dc chopper control flow.

D. Single Phase Inverter Output

The single phase inverter output circuit is to convert the DC bus voltage to an equivalent 60 Hz/110 V AC power source as shown in Fig. 16. The inverter is composed of a full bridge inverter composed of four IGBT switches in two arms, an input capacitor bank and output L-C low-pass filter. The major task of the inverter is to convert the DC voltage switched with high frequency to form a chopped AC waveform and then filtered by low-pass filter to smooth AC alternative power source to the load [21], [22].

The total system energy flow trend is illustrated in Fig. 17. The proposed system is an independent power generation system, not connected to the external power grid. To deliver a stable output power to the load through the single phase inverter, the power among the sub-system has to be balanced. The power distribution and balance algorithm is listed in Table III.

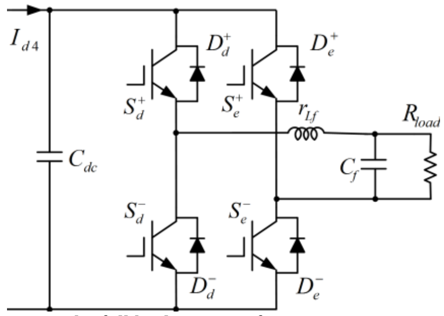

Fig. 16. The full bridge circuit for output power stage.

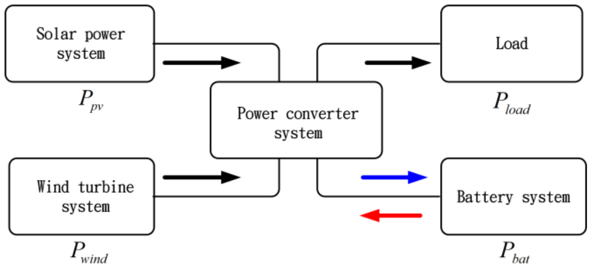

Fig. 17. The energy flow trends of the hybrid power generation system.

TABLE III: POWER DISTRIBUTION AND BALANCE ALGORITHM

Case	PV Power	Wind Power	Battery Power System
1	0	0	$P_{bat} = P_{load}$
2	$P_{pv} = P_{load}$	0	0
3	0	$P_{wind} = P_{load}$	0
4	$P_{pv} + P_{wind} = P_{load}$		0
5	$P_{pv} + P_{wind} > P_{load}$		$P_{bat} = P_{load} - P_{pv} - P_{wind}$ if negative, battery is charged
6	$P_{pv} + P_{wind} < P_{load}$		$P_{bat} = P_{load} - P_{pv} - P_{wind}$ If positive, battery is discharged.

IV. EXPERIMENTAL RESULTS

A. Solar Power Output Test

In Fig. 18, the PV module MPPT tracking profile is measured when MPPT is on. In the first 15 second, the duty cycle of the S_{pv} switch in the booster converter is varied and scanned to find the maximum power point to be use as MPPT tracking reference point, which is located at about 220 W. After 15 second, the Perturb and Observe algorithm is active, as shown in the Fig. 18, the maximum power point tracked is also about 220 W. This implies that the MPPT tracking strategy is proven to be correct. Fig. 19 shows the PV modules output voltage and current profile during 24 hours of measurement with sufficient sunshine. While in Fig. 20, the solar output power profiles with and without MPPT and Perturb and Observe algorithm are depicted. It is shown that the output power with MPPT and Perturb and Observe algorithm is near four times than that without MPPT and Perturb and Observe algorithm.

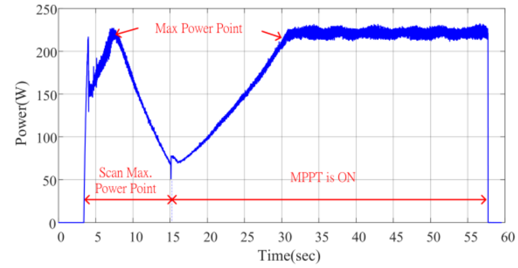

Fig. 18. the MPPT algorithm profile of solar power.

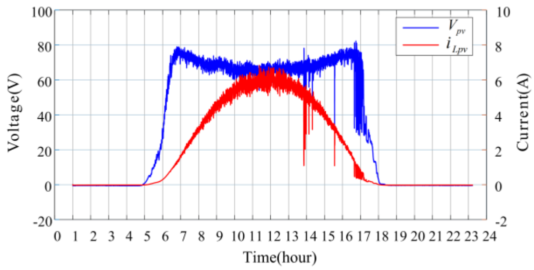

Fig. 19. Solar power voltage and current output profile during 24 hours.

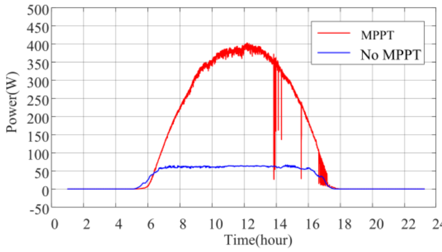

Fig. 20. Solar power output profile with/without MPPT during 24 hours.

B. *Wind Turbine Output Test*

In the wind power test, Chroma 6170, which is Programmable AC source delivers 3-phase AC power, is first used to simulate the wind power output. The power output varies with frequency from 20 to 120 Hz, with voltage 0 to 40V and the parameter change period is 250msec in order to test the SMR circuit's capability to correct the power factor for optimal operation.

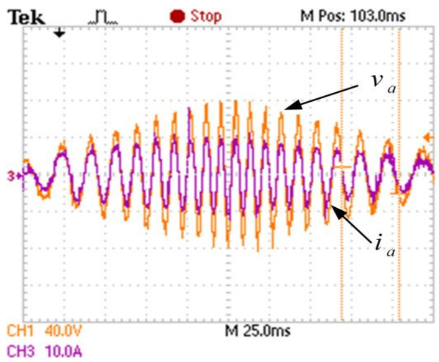

Fig. 21. Wind power output V-I curves with SMR active.

In the second phase of the test, a small wind turbine, Rutload 913 is adopted to verify the claimed optimal power factor correction and MPPT tracking with the simulation source. In fixed wind speed, the V-I curves using diode bridge and SMR circuit is shown in Fig. 22 and Fig. 23 respectively. As can be seen from Fig. 21, the diode bridge can only achieve 50 W output power with 0.939 power factor and total current harmonic distortion of 36.3%.

While in SMR circuit working with MPPT and Perturb and Observe algorithm, the achievable output power is 60 W with 0.998 power factor and total current harmonic distortion of 5.13%. Fig. 24 illustrates the wind turbine output power curves with diode and SMR. It is observed that, comparing to the traditional diode bridge, the output power is increased, the power factor is improved and the current harmonics is reduced. These all contribute to enhance the efficiency of wind power generation system. Fig. 25 and 26 demonstrate the single phase line voltage vs. the three phase current profiles before and after power factor correction with Wind turbine power factor correction algorithm describe in Section Ⅲ.B.2.

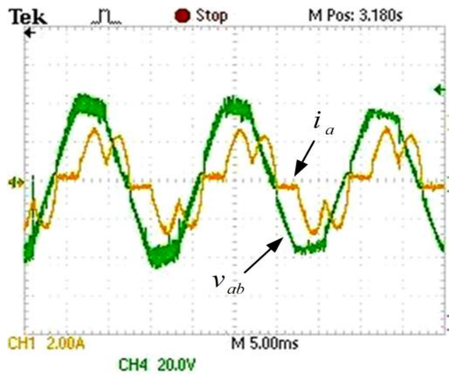

Fig. 22. Wind power output V-I curves with diode bridge rectifier.

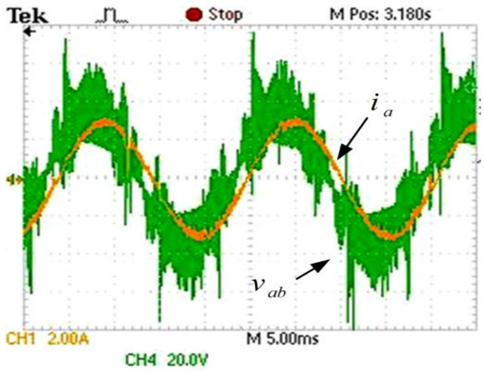

Fig. 23.the V-I curves of Wind turbine power output with SMR.

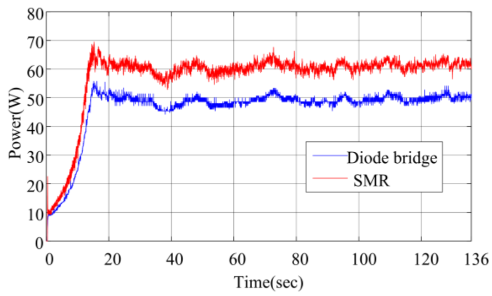

Fig. 24. Wind power output power with/without SMR.

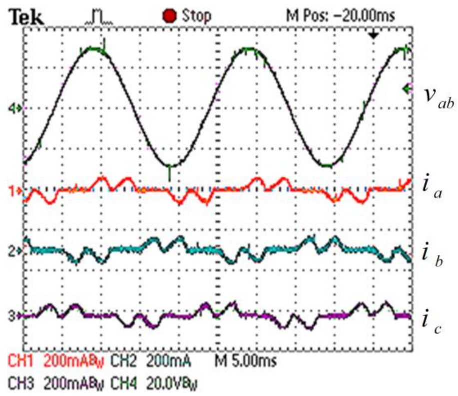

Fig. 25. Wind power output V-I curves without compensation.

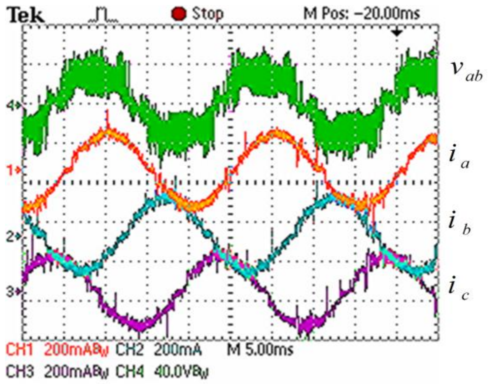

Fig. 26. Wind power output V-I curves with compensation.

The V-I curves variations due to the load change are also tested. In Fig. 27, the V-I curves are depicted when the load is change from 280W to lighter load 90 W, while in Fig. 28, the load change is reversed from 90W load to heavier load 280W.

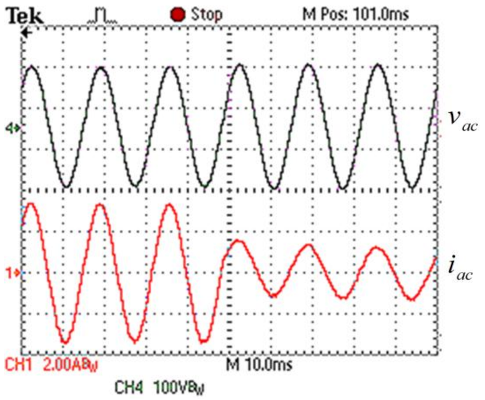

Fig. 27. Wind power output V-I curves with load disturbance from 280W to 90W.

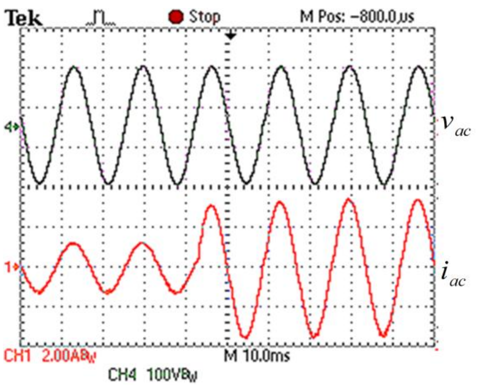

Fig. 28. Wind power output V-I curves with load disturbance from 90W to 280W.

Fig. 29 depicts the power output curves of the proposed hybrid system from 6 am to 21 pm. The power curve of the PV modules, wind turbine, battery system and load are included in the Figure. The power curve of each sub-system varies with time and is divided into four zones for convenient explanation of why the power curve varies with time, which the explanation is described as followed:

1) $0\sim t_1$

The load power needed is set as 90W. The solar power output is between 100W to 400W and the wind power output is around 0~400W. The total renewable power is larger than the load needs. To keep stable output power to load, the battery is operating in charge mode to store excessive solar and wind power energy.

2) $t_1\sim t_2$

The load power needed is increased from 90W to 240W. The total renewable power is also larger than the load needed. Hence, the battery is still operating in charge mode to store excessive energy.

3) $t_2\sim t_3$

The load power needed is 240W. During this period, the Δi_{Lpv} in Fig. 6 of the solar power Perturb and Observe algorithm is reduced to avoid large power variation. It is observed the solar power output varies smoothly in decreasing manner from 400W to 250W. In the period, the aggregated power by solar and wind is still larger than the load needs, the battery is still operating in charge mode.

4) $t_3\sim after$

The load power needed is 240W. The solar power output decreases with reduced sun irradiance, the aggregated power by solar and wind is under what the load needs, the battery is now operating in discharge mode to compensate the energy gap.

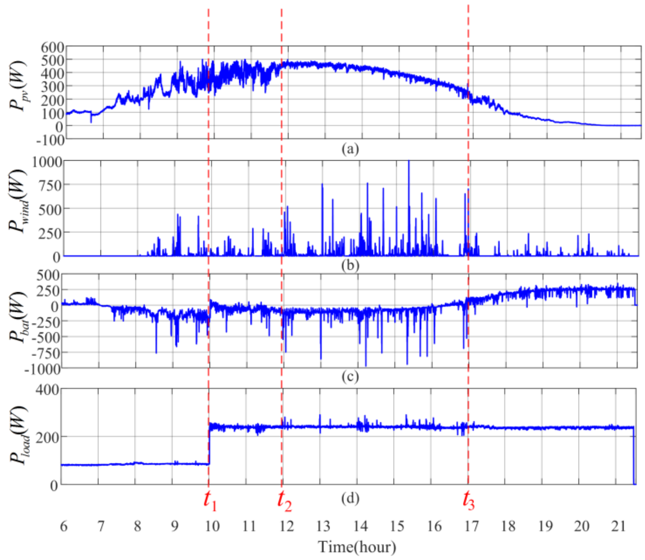

Fig. 29. Hybrid solar and wind system power output curves. (a) PV module power output (b) wind power output (c) battery power changes (d) load power variations.

When the battery cells are fully charged and the renewable power output is over what the load needs, the voltage of the DC bus will increase. This will endanger the proposed hybrid system. When this situation occur, the MPPT function for both the solar and wind power will be shut down, the battery will discharge and provide power to the load to avoid damage to the proposed hybrid system. Besides, when there is no sun irradiance and wind and the battery storage is below the safety low threshold, the inverter to the load will be stopped to protect the battery cells from over-discharging.

V. Conclusion

In this paper, a hybrid power generation system comprising solar, wind turbine and battery cells is introduced and implemented. It is demonstrated that the solar PV modules combined with DC/DC boost power converter and wind turbine combined with SMR converter work with MPPT and perturb and observe algorithm is capable of achieving MPPT tracking for both solar and wind power renewable energy. Besides, the power factor correction for wind turbine with SMR is a better structure than the traditional diode bridge, that can be improved the generation efficiency of wind turbine. All the MPPT algorithm and control strategy is implemented using digital signal processor (DSP, TMS320F2812), which is compact and easy to modify the control algorithm. Experimental results show that a stable and smooth operation of the hybrid renewable power system controlled by DSP processor is a feasible solution.

References

[1] H. Fargli, F. Fahmy, and M. EL-Sayed, "Artificial intelligence techniques for controlling PV-Wind," in *Proc. International Conference on Renewable Energies and Power Quality (ICREPQ'09). Valencia (Spain),* 2009.

[2] N. A. Ahmed and M. Miyatake, "A stand-alone hybrid generation system combining solar photovoltaic and wind turbine with simple maximum power point tracking control," in *Proc. Power Electronics and Motion Control Conference*, 2006, pp. 1-7.

[3] D. Shen, A. Izadian, and P. Liao, "A hybrid wind-solar-storage energy generation system configuration and control," in *Proc. Energy Conversion Congress and Exposition (ECCE)*, Pittsburgh, 2014, pp. 436-442.

[4] Y. M. Chen, Y. C. Liu, S. C. Hung, and C. S. Cheng, "Multi-input inverter for grid-connected hybrid PV/wind power system," *IEEE Transaction on Power Electronics,* vol. 22, pp. 1070-1077, 2007.

[5] C. Wang and M. H. Nehrir, "Power management of a stand-alone wind/ photovoltaic/fuel cell energy system," *IEEE Transactions on Energy Conversion,* vol. 23, pp. 957-967, 2008.

[6] M. A. S. Masoum, H. Dehbonei, and E. F. Fuchs, "Theoretical and experimental analyses of photovoltaic systems with voltage and current-based maximum power point tracking," *IEEE Transaction on Energy Conversion,* vol. 17, pp. 514-522, 2002.

[7] K. Harada and G. Zhao, "Controlled power interface between solar cells and AC source," *IEEE Transaction on Power Electronics,* vol. 8, pp. 654-662 1993.

[8] C. R. Sullivan and M.J. Powers, "A high-efficiency maximum power point tracker for photovoltaic arrays in a solar-powered race vehicle," in *Proc. Power Electronics Specialists Conference*, 1993, pp. 574-580.

[9] J. H. R. Enslin, "Maximum power point tracking: A cost saving necessity in solar energy systems," in *Proc. IEEE Ind. Electron Soc*, 1990, vol. 2, pp. 1073-1077.

[10] J. A. Gow and C. D. Manning, "Controller arrangement for boost converter systems sourced from solar photovoltaic arrays or other maximum power sources," in *Proc. IEE*, pp. 15-20, 2000, vol. 147.

[11] C. T. Pan, J. Y. Chen, C. P. Chu, and Y. S. Huang, "A fast maximum power point tracker for photovoltaic power systems," in *Proc. IEEE Ind.*, 1999, vol. 1, pp. 390-393.

[12] C. C. Hua and J. R. Lin, "Fully digital control of distributed photovoltaic power systems," *In Proc. IEEE Int.*, 2001, vol. 1, pp. 1-6.

[13] V. Vlatkovic and D. Borojevic, "Digital-signal-processor-based control of three-phase space vector modulated converters," *IEEE Trans. on Ind. Elec*., vol. 41, no. 3, pp. 326-332, June 1994.

[14] N. Femia, G. Petrone, G. Spagnuolo, and M. Vitelli, "Optimization of perturb and observe maximum power point tracking method," *IEEE Transactions on Power Electronics*, vol. 20, pp. 963-973, 2005.

[15] F. D. Aniel, R. Chaffai, and K. Al-Haddad, "A new modulation technique for reducing the input current harmonics of a three-phase diode rectifier with capacitive load," *IEEE Trans. on Ind. Appl.*, vol. 33, no. 5, pp. 1185-1193, Sept. 1997.

[16] E. L. M. Mehl and I. Barbi, "An improved high power factor and low cost three-phase rectifier," in *Proc. IEEE Applied Power Electronics Conference (APEC)*, 1995, vol. 2, pp. 835-841.

[17] V. Vlatkovic and D. Borojevic, "Digital-signal-processor-based control of three-phase space vector modulated converters," *IEEE Trans. on Ind. Elec*., vol. 41, no. 3, pp. 326-332, June 1994.

[18] J. W. Kolar and F. C. Zach, "A novel three-phase utility interface minimizing line current harmonics of high-power telecommunications rectifier modules," *IEEE Trans. on Ind. Appl*., vol. 44, no. 4, pp. 456-467, Aug. 1997.

[19] R. J. Tu and C. L. Chen, "A new three-phase space-vector-modulated power factor corrector," in *Proc. Applied Power Electronics Conference and Exposition*, pp. 725-730, 1994.

[20] M. Jain, "A bidirectional dc–dc converter topology for low power application," *IEEE Transactions on Power Electronics*, vol. 15, no. 4, July 2000.

[21] S. Nonaka, "A utility-connected residential PV system adapted a novel single-phase composite PWM voltage source inverter," in *Proc. IEEE WCPEC*, vol. 1, pp. 1064-1068, 1994.

[22] S. Nonaka and Y. Neba, "Single-phase composite PWM voltage source converter" in *Proc. IEEE WCPEC*, 1994, vol. 2, pp. 761-768.

Bao-Sheng Wang received the B.Sc. and M.Sc. degrees of electrical engineering from National Taiwan University of Science and Technology, Taipei, Taiwan, in 2006 and 2009. Since 2009, he has been with the Power Supply Group, Department of Light Source, National Synchrotron Radiation Research Center, Hsinchu, Taiwan. His current research interests include power electronics, control theory and process control.

Chen-Yao Liu received the B.Sc. and M.Sc. degrees from National Chiao Tung University, Hsinchu, Taiwan, in 1992 and 1994, respectively, all in control engineering. Since 1996, he has been with the Power Supply Group, Department of Light Source, National Synchrotron Radiation Research Center, Hsinchu, Taiwan. His current research interests include power electronics technology, particle accelerator power supplies system and other related topics.

Kuo-Bin Liu received the B.Sc. and M.Sc. degrees from National Chiao Tung University, Hsinchu, Taiwan, in 1988 and 1990, respectively, all in control engineering. Since 1990, he has been with the Power Supply Group, Department of Light Source, National Synchrotron Radiation Research Center, Hsinchu, Taiwan. His current research interests include power electronics technology, particle accelerator power supplies system and other related topics.

Yuan-Chen Chien received the B.Sc. and M.Sc. degrees of control engineering from National Chiao Tung University, Hsinchu, Taiwan respectively in 1992 and 1994. He is assistant engineer of the Power Supply Group, Department of Light Source, National Synchrotron Radiation Research Center, Hsinchu, Taiwan since 1996. His current research interests include embedded controller design, power converter architecture and FPGA design.